Contents lists available at ScienceDirect

Applied Catalysis B: Environmental

Core-shell nickel catalysts for the steam reforming of acetic acid

Jianglong Pu, Katsuki Nishikado, Ningning Wang, Thanh Tung Nguyen, Tei Maki, Eika W. Qian*

Graduate School of Bio-Applications and Systems Engineering, Tokyo University of Agriculture and Technology, 2-24-16, Nakacho, Koganei, Tokyo 184-8588, Japan
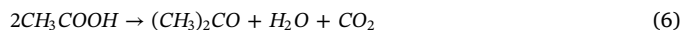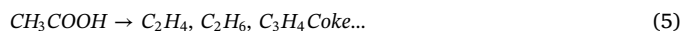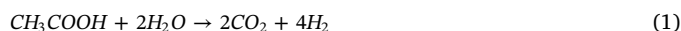
ARTICLE INFO

ABSTRACT

To obtain a novel catalyst with high resistances to metal sintering and coke formation in the steam reforming of acetic acid, a series of nickel core-shell catalysts were prepared. The effects of the shell thickness, shell species and core particle size on the catalytic activity in the steam reforming of acetic acid were investigated. The prepared Ni@SiO$_2$, Ni@Al$_2$O$_3$, Ni@CeO$_2$ and Ni@TiO$_2$ catalysts were characterized by BET, XRD, H$_2$-TPR, DTG and HRTEM. The prepared core-shell catalysts showed high resistances to nickel sintering, owing to the protection of the shells, in comparison with bare nickel particles. Ni@SiO$_2$ with a thin shell showed a higher activity than the corresponding catalyst with a thick shell due to the thin silica shell allowing the facile diffusion of reactants and products. Because of the important role of the support in steam reforming reactions, the shell species greatly affected the catalytic activity in the steam reforming of acetic acid. It was demonstrated that an alumina shell was best suited for the steam reforming of acetic acid among the studied shells owing to its excellent water dissociation ability. The Ni@Al$_2$O$_3$-i catalyst showed excellent activity with an almost complete conversion and a hydrogen yield up to 91.2% at 750 °C due to its much smaller nickel particle size. The coke formed on the spent core-shell catalysts after the activity tests was mainly graphic carbon, and the Ni@Al$_2$O$_3$-i catalyst exhibited a superior coke resistance with the smallest amount of formed coke. HRTEM results of Ni@Al$_2$O$_3$-i indicated the alumina shell had a high hydrothermal stability and further confirmed the high sintering resistance in the steam reforming of acetic acid.

1. Introduction

Because of the decreasing supply of fossil fuels, global warming resulting from the excessive emission of carbon dioxide and increasing demand for energy [1,2], the utilization of renewable and alternative resources from biomass has attracted increasing attention from researchers. Fast pyrolysis is one of the most widely used technologies to convert biomass into bio-oil [3]. Due to the rather complex composition of bio-oil, which greatly depends on the conditions of pyrolysis and the source of biomass, bio-oil needs to be further upgraded. Steam reforming of bio-oil is a promising approach to convert the energy stored in biomass into easily usable hydrogen. Although the well-established technology of catalytic steam reforming of methane has been commercialized for many years [4], hydrogen production via steam reforming of bio-oil still faces many challenges due to the more complex composition of bio-oil [5,6]. Moreover, the complex composition of bio-oil also easily results in the formation of coke on the catalyst. A relatively large amount of acetic acid exists in bio-oil and it is also notorious for the coke formation on the catalyst [7–9], therefore, many researchers are focusing on the steam reforming of acetic acid (SRAA) [5,7,10–12]. The steam reforming of acetic acid occurs simultaneously

with the water gas shift (WGS) reaction (Eq. (2)) and the overall reaction is represented as Eq. (1). The main side reactions in the steam reforming of acetic acid are decomposition reactions of acetic acid (Eqs. (3)–(5)), as well as the ketonization of acetic acid (Eq. (6)), by which the formed acetone is considered to be a coke precursor [13,14]. The acetic acid is unstable at temperatures from 500 °C to 800 °C, where coke is easily formed by thermal decomposition (Eq. (5)). The severe hydrothermal environment of steam reforming of acetic acid makes the catalyst easily lose its activity due to the sintering of metallic particles and coke deposition on the active sites [9,15,16].

$$CH_3COOH + 2H_2O \rightarrow 2CO_2 + 4H_2 \qquad (1)$$

$$CO + H_2O \rightleftharpoons CO_2 + H_2 \qquad (2)$$

$$CH_3COOH \rightleftharpoons 2CO + 2H_2 \qquad (3)$$

$$CH_3COOH \rightleftharpoons CH_4 + CO_2 \qquad (4)$$

$$CH_3COOH \rightarrow C_2H_4, C_2H_6, C_3H_4 Coke... \qquad (5)$$

$$2CH_3COOH \rightarrow (CH_3)_2CO + H_2O + CO_2 \qquad (6)$$

Supported noble metal catalysts, such as Ru, Rh, Pt and Ir, show

* Corresponding author.
  E-mail address: whqian@cc.tuat.ac.jp (E.W. Qian).

high catalytic activities and good stabilities [17–20]. The studies of acetic acid steam reforming over the Rh and Ru supported catalysts implied that acetic acid was well reformed on metallic surfaces, while on defective sites, like an interface or the periphery of the metallic crystallites, the coke formation was favored [19,20]. On the other hand, Ni-based catalysts, which are low cost and show high C−C cleavage activities, are more suitable for economic interests [21]. Therefore, many researchers have devoted studying Ni-based catalysts in steam reforming reactions [22–25]. However, compared to noble metal catalysts, Ni-based catalysts are more prone to sintering and coke deposition due to the relatively large loading of nickel. The studies on the coke formation mechanism in the steam reforming reactions over Ni-based catalysts indicated that catalyst deactivation was mainly due to encapsulating nonfilamentous carbon, which blocked the nickel active sites [16,26]. However, the filamentous carbon formed from CO and CO_2 did not lead to catalyst deactivation, rather only resulted in detachment of the nickel active sites from the support [26]. Thus, to inhibit coke formation in the steam reforming of acetic acid, a high acetic acid conversion is necessary, which can greatly decrease the accumulation of the precursor for nonfilamentous carbon. Although an increased steam to carbon ratio and temperature are favored to attenuate coke formation by accelerating coke gasification reactions [27], catalyst deactivation occurs from the sintering of nickel metal, and energy costs will also increase accordingly. Extensive methods have been employed to enhance the coke resistance of catalysts and prevent Ni particles from agglomerating at high temperatures, including confining the Ni particles in porous materials [28], improving the Ni dispersion on the support [29], developing the materials with strong interaction between the Ni nanoparticles and support such as perovskite and spinel [29], employing bimetallic catalysts to form alloys [30,31], introducing oxide promoters onto the supports [26], and coating inorganic shells on the surface of nickel [32,33].

Recently, a Ni@SiO$_2$ catalyst with a core-shell structure has been widely used for methane dry reforming, CO methanation and methane partial oxidation reactions, showing good sintering resistance due to the protection of the robust silica shell, as well as an excellent coke resistance by restricting the formation of coke [34–37]. Previous research indicated that the silica-encapsulated Ni nanoparticles significantly suppressed sintering and coking, which resulted in excellent activity and stability after a 40-h activity test for the dry reforming of methane with only negligible coke formation [34]. Moreover, the porous structure of the silica shell is greatly influenced by the type of surfactant template, for instance, an ordered mesoporous silica shell was formed using hexadecyltrimethylammonium bromide (CTAB) as a template, while disordered mesopores were formed by adding n-octadecyltrimethoxysilane [38]. For methane dry reforming, TiO$_2$-coated Ni particles also exhibited superior stability after a 160-h long-term operation in comparison to bare Ni particles [39].

Although excellent coking and sintering resistances have been achieved, there have been few studies on core-shell catalysts in steam reforming reactions. Since great differences result from various reaction conditions, types of reactants and reaction mechanisms, which particularly have important roles on water dissociation from the supports [40], it is necessary to find the type of shell that is best fitted for the steam reforming of acetic acid.

Therefore, in the present study, with the aim to develop a Ni-based core-shell catalyst with high activity and good stability, the effects of shell species, shell thickness and Ni particle size on the catalytic activity in the steam reforming of acetic acid were investigated. First, Ni particles encapsulated with SiO$_2$, CeO$_2$, TiO$_2$ and Al$_2$O$_3$ were prepared to investigate the effect of the shell species. Then, the effect of the silica thickness was investigated by adjusting the amount of tetraethyl orthosilicate. To investigate the effect of the particle size, Ni particles were synthesized using two methods. The catalytic activities in the steam reforming of acetic acid were studied in a fixed-bed flow reactor. Finally, the sintering and coking resistance of these prepared catalysts

were compared. In addition, the possible correlations among the shell species, thickness, porous structure and catalytic activity in the steam reforming of acetic acid were elucidated.

2. Experimental

2.1. Materials

Nickel chloride hexahydrate (NiCl$_2$·6H$_2$O, > 98%, Wako), hydrazine monohydrate (N$_2$H$_4$·H$_2$O, > 97%, Wako), sodium borohydride (NaBH$_4$, > 98%, Sigma-Aldrich), polyvinylpyrrolidone (K = 27.0–32.4, Wako), hexadecyltrimethylammonium bromide (CTAB, > 98%, Tokyo Chemical Industry), sodium hydroxide (NaOH, > 97%, Kishida Chemical), ethylene glycol (EG, > 99.5%, Wako), tetraethyl orthosilicate (TEOS, > 95%, Wako), titanium ethoxide (technical grade, Sigma-Aldrich), cerium nitrate hexahydrate (Ce(NO$_3$)$_3$·6H$_2$O, > 98%, Wako), urea (> 99%, Wako), and aluminum isopropoxide (> 98%, Sigma-Aldrich) were used as received without further purification.

2.2. Catalyst preparation

2.2.1. Synthesis of the nickel particles

The Ni particles were synthesized by the reduction of Ni^{2+} using N$_2$H$_4$·H$_2$O as a reductant and EG as a solvent [41]. NiCl$_2$·6H$_2$O (3.57 g) was added to a three-neck flask and dissolved in EG at room temperature, followed by 5 min of ultrasonication. NaOH (0.90 g) was added to a beaker and dissolved in EG with magnetic stirring. Then, N$_2$H$_4$·H$_2$O (13.95 ml) was added to the NiCl$_2$ solution with vigorous mechanical stirring. Approximately 1 min later, the NaOH solution was added, and a blue precursor was formed in the suspension. The concentration of Ni^{2+}, hydrazine and OH$^-$ was kept at 0.05 M, 1 M and 0.075 M, respectively. The reduction reaction was conducted at 120 °C with vigorous stirring for 15 min. The obtained black precipitate was separated by centrifugation and washed with distilled water until the pH was 7. Finally, the samples were washed 3 times with ethanol and dried in air at room temperature overnight.

2.2.2. Synthesis of the Ni@SiO$_2$ catalyst

The SiO$_2$ shell was coated on the Ni particles using the Stöber method [34,35]. Generally, the Ni particles (0.30 g) were dispersed in a solution with 225 ml of ethanol and 150 ml of distilled water. Subsequently, a 25% ammonia solution (4 ml) and CTAB (0.68 g) were added to the solution, followed by 5 min of ultrasonication. The suspension was stirred vigorously at room temperature for 30 min. TEOS (0.3 ml or 3.0 ml) was added to the solution for the thin- or thick-shell catalyst, respectively. The suspension was kept at 60 °C with vigorous stirring for 6 h. The obtained powder was washed 3 times with ethanol and once with a 6 g/L NH$_4$NO$_3$/ethanol solution to remove impurities. Finally, the powder was dried at room temperature overnight. The catalysts with a thin and thick silica shell are designated as Ni@SiO$_2$ and Ni@SiO$_2$-T, respectively.

2.2.3. Synthesis of the Ni@TiO$_2$ catalyst

The Ni particles (0.20 g) and CTAB (0.45 g) were dispersed in 50 ml of anhydrous ethanol in a flask, followed by 1 h of ultrasonication. Subsequently, titanium ethoxide (0.12 g) was quickly added to the suspension. The suspension was vigorously stirred overnight in the tightly closed flask. Distilled water (3 ml) diluted with 6 ml of ethanol was added dropwise to the suspension. The suspension was aged for 1 h with vigorous stirring. The particles were treated with water at 105 °C for 24 h to crystallize the TiO$_2$ shell. Finally, the catalyst was calcined at 600 °C for 6 h.

2.2.4. Synthesis of the Ni@CeO$_2$ catalyst

The Ni particles (0.20 g) and CTAB (0.45 g) were dispersed in 50 ml of anhydrous ethanol, followed by 1 h of ultrasonication. Subsequently,

$Ce(NO_3)_3 \cdot 6H_2O$ (0.1 g) was added to the suspension. A urea solution was dropped into the suspension quickly at 90 °C with vigorous stirring. The $Ce(OH)_3$ precipitate was coated on the Ni particles under alkaline conditions by the slow decomposition of urea. Finally, the particles were washed and calcined at 600 °C for 6 h.

2.2.5. Synthesis of the Ni@Al₂O₃ catalyst

Ni particles (0.20 g) and CTAB (0.45 g) were dispersed in 50 ml of anhydrous ethanol, followed by 1 h of ultrasonication. Aluminum isopropoxide (0.14 g) was added to the suspension. Distilled water (5 ml) was dropped into the suspension with vigorous stirring. The suspension was kept at room temperature for 24 h. Finally, the particles were washed and calcined at 600 °C.

2.2.6. Synthesis of the improved Ni@Al₂O₃ catalyst

To prepare the Ni particles with a smaller size, the nickel precursor was reduced by $NaBH_4$ [42]. Typically, 4.05 g of $NiCl_2 \cdot 6H_2O$ and 0.40 g of PVP were dispersed in 600 ml of distilled water, followed by 15 min of ultrasonication. Subsequently, 2.0 g of $NaBH_4$ dissolved in 200 ml of distilled water was dropped slowly into the suspension at room temperature with vigorous stirring. The black precipitate was separated by centrifugation and washed until the pH was 7. The coating method for the Al_2O_3 shell was the same as that for the conventional Ni@Al₂O₃ catalyst. The improved Ni@Al₂O₃ catalyst is designated as Ni@Al₂O₃-i.

2.3. Catalyst characterization

The physical properties of the catalysts (BET surface area, pore volume and pore diameter) were measured from N_2 adsorption-desorption isotherms at liquid nitrogen temperature (-196 °C), obtained by a Belsorp-mini II analyzer (Bel Japan Inc.). The samples were outgassed at 400 °C for 1 h before analysis.

X-ray fluorescence (XRF) analysis of the catalysts was conducted with an XRF spectrometer (JSX-3100RII, JEOL Corp.) to quantify the amount of the shell species.

X-ray diffraction (XRD) analysis of the catalysts was performed with an XRD instrument (RINT2100 VPC/N, Rigaku Corp.) with Cu-Kα radiation (40 kV, 30 mA). The crystallite sizes of NiO (for the calcined catalysts) and Ni^0 (for the reduced catalysts) were calculated by applying the Scherrer equation to their corresponding peaks.

Hydrogen temperature-programmed reduction of the catalysts was performed in a chemisorption-physisorption analyzer (ChemBET PULSAR TPR/TPD; Quantachrome Instruments). Typically, approximately 100 mg of a sample was loaded into the quartz U-tube. Prior to analysis, the samples were pretreated with helium at 500 °C for 1 h. Subsequently, the H_2-TPR analysis was performed from ambient temperature to 900 °C with a heating rate of 5 °C/min. The consumption of H_2 was monitored online with a TCD detector.

Scanning electronic microscopy (SEM) of synthesized Ni particles was carried out with a JSM-6510 microscope (JEOL Corp.) to determine the surface morphologies.

High resolution transmission electron microscopy (HRTEM) images were obtained using a JEM-2200FS microscope (JEOL Corp.) operating at 200 kV with an EDS detector. The samples were dispersed in ethanol, and a drop of the suspension was deposited onto a carbon-coated copper microgrid (JEOL Corp.). Prior to analysis, the sample was dried at 60 °C for 1 h.

Thermal gravimetric analysis (TGA) of the spent catalysts after the activity tests was performed with a TA instrument (TGA, TA-60WS, SHIMADZU). Approximately 10 mg of a sample was combusted under an air flow from ambient temperature to 900 °C with a heating rate of 10 °C/min.

2.4. Catalytic activity tests

The catalytic activity tests of the catalysts were carried out in a fixed-bed flow reactor (8 mm internal diameter; 350 mm length). Approximately 150 mg of a catalyst was diluted with quartz sand and loaded into the constant-temperature zone of the reactor. Before the reaction, the catalyst was reduced by pure H_2 (100 ml/min) at 600 °C for 3 h. Water and acetic acid were continuously fed by two pumps kept a molar ratio of steam to carbon of 3.18. N_2 (150 ml/min) was used as the carrier gas controlled by a mass flowmeter (8500MC). Steam reforming of acetic acid was conducted at 650, 700, 750 °C under atmospheric pressure. The weight hourly space velocity (WHSV) of acetic acid for each experiment was kept at 21 h^{-1}. The gas and liquid in the outlet of the reactor were separated by a flash condenser. The composition of H_2 was quantified by a gas chromatograph (SHIMADZU GC-8A) with a TCD detector using N_2 as the carrier gas. The other compositions were quantified by a gas chromatograph (SHIMADZU GC-8A) with a TCD detector using helium as the carrier gas. The unreacted acetic acid in the residual liquid was quantified by GC-FID (GC–14 B SHIMADZU).

The conversion of acetic acid was calculated according to the equation below:

$$X_{AA}(\%) = \frac{\text{acetic acid feed} - \text{unreacted acetic acid}}{\text{acetic acid feed}} \times 100\%$$

The yield of H_2 was defined by the stoichiometric H_2 formation:

$$Y_{H_2}(\%) = \frac{\text{moles of hydrogen produced}}{4 \times \text{moles of acetic acid feed}} \times 100\%$$

The selectivity of the carbonaceous products (CO, CH_4 and CO_2) was estimated on a carbon basis:

$$S_C(\%) = \frac{\text{moles of carbon of each carbonaceous product}}{2 \times \text{moles of reacted acetic acid feed}} \times 100\%$$

3. Results and discussion

3.1. Characterization of the properties of the core-shell catalysts

3.1.1. Textural features

The SEM images of the nickel particles prepared using different reductants are presented in Fig. 1. In the case of hydrazine monohydrate (Fig. 1a), nickel particles with a uniform spherical morphology were obtained, and the mean diameter of the synthesized nickel particles was approximately 250 nm. In the case of $NaBH_4$ (Fig. 1b), much smaller nickel nanoparticles with a spherical morphology were obtained.

The BET pore volume, surface area and pore diameter of the prepared catalysts are listed in Table 1. Based on the shell species, the core-shell catalysts showed different porous shell structures. Because of the small amount of shell species on the catalysts, all the core-shell catalysts showed lower surface areas than the conventional catalysts. Among the catalysts with the same nickel particle size and similar amount of shell species, the Ni@SiO₂ catalyst showed the largest surface area (52.8 $m^2\,g^{-1}$) with a pore volume of 12.1 $cm^3\,g^{-1}$ and pore diameter of 3.4 nm, indicating the SiO₂ shell has the most porous structure. Similarly, due to the highly porous structure of Al_2O_3, the Ni@Al₂O₃ catalyst also had a relatively large surface area and pore volume. In contrast, the Ni@CeO₂ and Ni@TiO₂ catalysts showed the least porous structures with surface areas of 13.0 and 14.4 $m^2\,g^{-1}$, respectively.

In addition, due to the thicker SiO₂ shell, the Ni@SiO₂-T catalyst showed a much larger surface area (200.5 $m^2 \cdot g^{-1}$) than Ni@SiO₂. Meanwhile, the pore volume of Ni@SiO₂-T also increased to 46.1 $m^2 \cdot g^{-1}$, indicating an increase in the thickness of the porous silica shell upon adding more TEOS.

Compared with Ni@Al₂O₃, the surface area of the Ni@Al₂O₃-i catalyst (180.5 $m^2\,g^{-1}$) was also greatly increased by the much smaller Ni particle size. This is because the smaller Ni particles had a larger contact surface area with the Al_2O_3 shell, which dramatically enhanced the

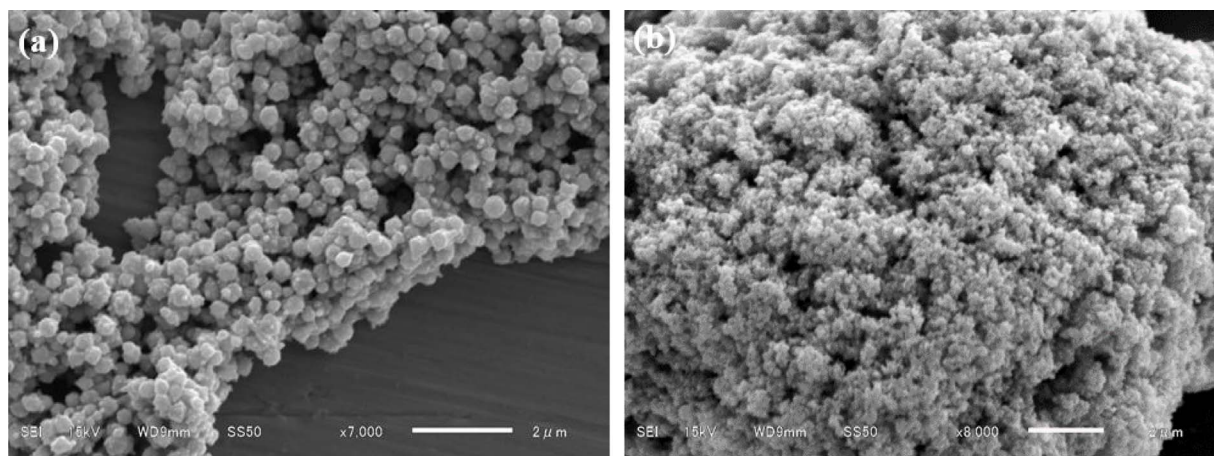Fig. 1. SEM images of the synthesized Ni particles using (a) N$_2$H$_4$·H$_2$O and (b) NaBH$_4$ as reductants.

Table 1
Physical properties of the prepared core-shell catalysts.

Catalyst	V_m (cm^3 g^{-1})[a]	A_s (m^2 g^{-1})[b]	d (nm)[c]
Ni@SiO$_2$	12.1	52.8	3.4
Ni@SiO$_2$-T	46.1	200.5	2.3
Ni@TiO$_2$	3.3	14.4	13.5
Ni@CeO$_2$	3.0	13.0	14.1
Ni@Al$_2$O$_3$	10.2	44.2	7.0
Ni@Al$_2$O$_3$-i	41.5	180.5	3.6

[a] Pore volume.
[b] surface area.
[c] pore diameter of the catalysts derived from nitrogen isothermal adsorption and desorption measurements.

coating of the Al$_2$O$_3$ shell. Accordingly, the Ni@Al$_2$O$_3$-i (41.5 cm^3 g^{-1}) catalyst showed a larger pore volume than Ni@Al$_2$O$_3$ (10.2 cm^3 g^{-1}).

The XRD patterns of the calcined and reduced core-shell catalysts are presented in Fig. 2. The NiO crystal phase (JCPDS: 73-1523) is shown for the two types of calcined nickel particles (Fig. 2a). Besides the diffraction peaks corresponding to the NiO phase, no other diffraction peaks were found in the calcined NiO XRD patterns. All these core-shell catalysts showed strong diffraction peaks corresponding to the NiO phase, indicating the large amount of nickel oxide. The diffraction peaks corresponding to the CeO$_2$ phase were detected for Ni@CeO$_2$ but were much weaker in comparison with the diffraction peaks corresponding to NiO, suggesting the small amount of the CeO$_2$ shell species. In contrast, the shell species of the other core-shell catalysts, i.e., Ni@SiO$_2$, Ni@Al$_2$O$_3$ and Ni@TiO$_2$, were not detected by XRD due to the small amounts of the shell species and possibly the poor crystallinities. This also demonstrates that CeO$_2$ has better crystallinity than the other shell species. In addition, unlike the sharp and strong NiO diffraction peaks of the normal catalysts, the calcined Ni particles synthesized using NaBH$_4$ and the improved Ni@Al$_2$O$_3$ catalyst showed wide and weak NiO peaks due to the much poorer crystallinities.

The diffraction peaks corresponding to a Ni phase were observed for all the reduced catalysts, indicating the conversion of NiO to metallic nickel during the reduction (Fig. 2b). Similar to the results of the calcined catalysts, only CeO$_2$ peaks for the Ni@CeO$_2$ catalyst were detected. The improved Ni and Ni@Al$_2$O$_3$-i catalysts showed wider and weaker peaks in comparison with the other catalysts. It is noteworthy that the Ni diffraction peaks of Ni@Al$_2$O$_3$-i are much weaker than those of Ni-i after reduction, even though the XRD patterns for the two calcined catalysts are similar, as presented in Fig. 2a. This indicates that the Ni particle size in Ni-i becomes much bigger than that of Ni@Al$_2$O$_3$-i after reduction; however, the NiO particles in both the calcined NiO-i and Ni@Al$_2$O$_3$-i catalysts have similar sizes. It was suggested that the Ni particles in NiO-i suffered from severe agglomeration during the reduction, but the sintered Ni particles in Ni@Al$_2$O$_3$-i were greatly inhibited by the protection of the Al$_2$O$_3$ shell.

To further investigate the ability of the core-shell catalysts to inhibit nickel sintering, the NiO and Ni crystallite sizes were calculated from the XRD patterns (Table 2). For all cases, the samples underwent the same temperature ramping rate, i.e., 20 °C/min, from ambient temperature. The NiO particles synthesized using NaBH$_4$ exhibited a much
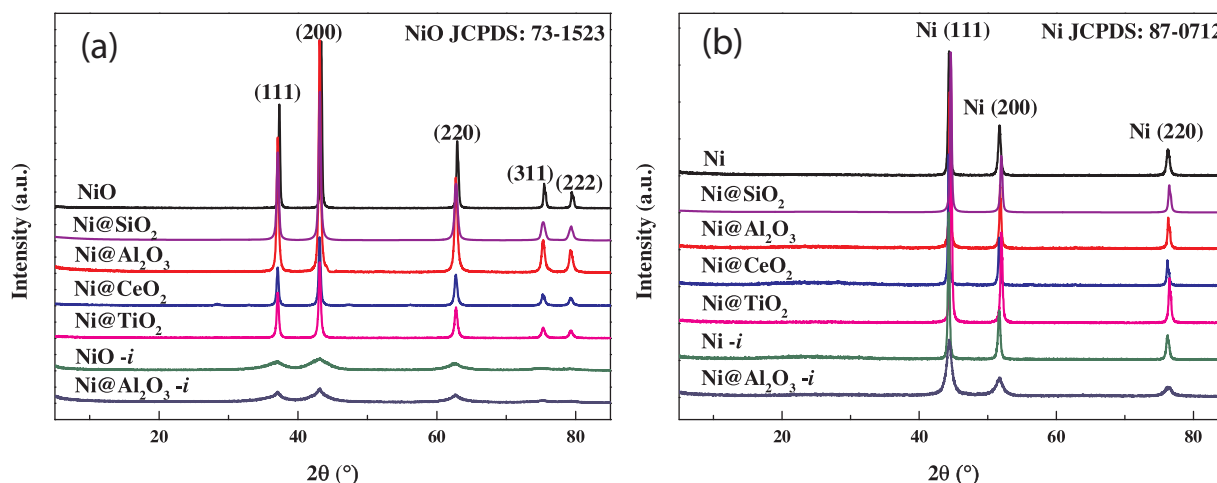

Fig. 2. XRD patterns of the (a) calcined and (b) reduced Ni particles and catalysts. Reduction temperature: 600 °C.

Table 2
Chemical compositions of the core-shell catalysts measured by XRF, and the Ni crystallite sizes before and after reduction at 600 °C.

Catalyst	NiO (wt%)	Shell species (wt%)	d_c (nm)	d_r (nm)
Ni	–	–	25.3	59.2
Ni@SiO$_2$	98.1	1.9	25.9	40.7
Ni@SiO$_2$-T	92.4	7.6	26.8	41.3
Ni@Al$_2$O$_3$	95.2	4.8	27.3	42.7
Ni@CeO$_2$	97.6	2.4	26.3	42.3
Ni@TiO$_2$	97.7	2.3	25.4	39.1
Ni-i	–	–	3.5	32.1
Ni@Al$_2$O$_3$-i	94.4	5.6	4.1	8.5

d_c, d_r: Ni particle sizes after calcination and reduction, respectively, which were estimated from XRD.

smaller crystallite size (3.5 nm) than those synthesized using hydrazine (25.3 nm). Nevertheless, the Ni particle size increases dramatically after reduction at 600 °C for all samples, indicating that nickel suffers from severe sintering. In contrast, the Ni crystallite sizes of the core-shell catalysts only showed slight increases after reduction, suggesting that the shell species greatly protect the Ni particles from sintering during reduction. It is concluded that the core-shell catalysts prepared show a good ability to inhibit nickel sintering.

3.1.2. Identification of the core-shell structure

The chemical compositions of the catalysts quantified by XRF are listed in Table 2. The compositions of the shell species were all detected by XRF, indicating the shell species were successfully coated onto the catalysts; however, the definite structures and morphologies of the shell species should be further determined. The compositions of the shell species are slightly different for the various catalysts due to the different preparation methods. As expected, much more SiO$_2$ was detected for Ni@SiO$_2$-T, suggesting a much thicker SiO$_2$ shell than that in Ni@SiO$_2$.

To further understand the detailed core-shell structures, TEM images of the reduced catalysts with the different types of shell species were obtained (Fig. 3). Overall, the core-shell structures were observed for all the catalysts. Amorphous silica with a thickness of approximately 50 nm was uniformly coated on the surface of the Ni particles by the hydrothermal decomposition of TEOS (Fig. 3a). It is shown that the silica shell has a porous structure, which is in accordance with the BET results, where the Ni@SiO$_2$ catalyst had the largest surface area and pore volume. As shown in Fig. 3b, the Ni particles were also encapsulated by amorphous alumina in the Ni@Al$_2$O$_3$ catalyst; however, the formed alumina shell was not as uniform as the silica shell. A small amount of alumina agglomerated in the vicinity of the Ni@Al$_2$O$_3$ particles. Additionally, the formed alumina shell had a highly porous structure, which explains the relatively large surface area and pore volume, as listed in Table 1. In contrast, from the TEM images (Fig. 3c and d), it was shown that the Ni@CeO$_2$ and Ni@TiO$_2$ catalysts have smooth shells, suggesting poor porous shell structures corresponding to the relatively small surface areas and pore volumes. The uneven shell structures for the Ni@Al$_2$O$_3$, Ni@CeO$_2$ and Ni@TiO$_2$ catalysts may due to the rapid decomposition of the precursors and their uneven adsorption on the nickel surface. As shown in Fig. 3d, TiO$_2$ with different sizes was agglomerated in the vicinity of the Ni particles. CeO$_2$ crystallites coated on the Ni particles was also evidenced by the appearance of the relatively weak diffraction peaks in Fig. 2.

The core-shell structure of the Ni@Al$_2$O$_3$-i catalyst was observed by HRTEM. As shown in Fig. 4a, the size of the Ni particles greatly decreased by using the reductant NaBH$_4$. In accordance with the strong diffraction peaks of nickel, the crystallinity was also reflected in the HRTEM image. Amorphous alumina was uniformly coated on the surface of the Ni particles. Moreover, the thickness of the alumina shell was approximately 3 nm, which will allow easier diffusion of the

reactants and products. The porous structure of the alumina shell was also well evidenced by the TEM image. The Ni particle size distribution of the Ni@Al$_2$O$_3$-i catalyst is shown in Fig. 4b. The Ni particle size was concentrated at approximately 10 nm, and the average size was 10.21 nm, which is more than 20 times smaller than those of the Ni@Al$_2$O$_3$ catalyst synthesized using hydrazine. The much smaller Ni particles provide more contact surface area for the coating of alumina. The increased contact surface area of the Ni particles and the highly porous structure of the amorphous alumina explains the much larger surface area and pore volume of the improved Ni@Al$_2$O$_3$ catalyst in comparison with the ordinary core-shell catalysts.

The STEM image and EDS mappings of the fresh Ni@Al$_2$O$_3$-i catalyst are shown in Fig. 5. The elements in the catalyst were distinguished by the EDS detector of the TEM instrument. As shown in Fig. 5b, the red sections corresponding to nickel were focused in the center of the particles, suggesting that the core of Ni@Al$_2$O$_3$-i consists of nickel. Meanwhile, the green sections corresponding to aluminum were distributed all over these particles, particularly around the periphery of the particles where the concentration of aluminum is higher (Fig. 5c). This indicates the shell of Ni@Al$_2$O$_3$-i is comprised of alumina. It is easy to distinguish the core-shell structure of Ni@Al$_2$O$_3$-i when all these elements are overlaid in Fig. 5d.

3.1.3. Reducibilities of the catalysts

H$_2$-TPR was performed to investigate the reducibility of nickel oxide and the interaction between nickel and the shell species. As shown in Fig. 6, peaks of hydrogen consumption corresponding to the reduction of NiO for the Ni@SiO$_2$, Ni@CeO$_2$, Ni@Al$_2$O$_3$ and Ni@TiO$_2$ core-shell catalysts appeared from 357 °C to 600 °C. It is shown that the shell species considerably affected the reduction of NiO due to the porous structure of the shell and the interaction between the core and shell. The NiO reduction peak of the Ni@Al$_2$O$_3$ catalyst was centered at 495 °C, which was lower than that of Ni@TiO$_2$ (521 °C) and Ni@SiO$_2$ (505 °C), suggesting the better reducibility of Ni@Al$_2$O$_3$. This may be due to the porous structure of the amorphous alumina providing a smaller hindrance for hydrogen diffusion to the core surface than for the TiO$_2$ and SiO$_2$ shells. The Ni@CeO$_2$ catalyst shows two peaks corresponding to the reduction of NiO at 452 °C and the partial reduction of CeO$_2$ at 570 °C [43]. Affected by the CeO$_2$ shell species, the reduction of NiO appeared at a low temperature. This may be explained by the facile redox properties of CeO$_2$, which accelerated the reduction of NiO [43]. On the other hand, Ni@Al$_2$O$_3$-i shows a broad reduction peak from 366 °C to 820 °C due to the much smaller nickel particles with a large contact surface area having a strong interaction with the alumina shell. According to previous studies about the Ni-based catalysts using alumina as support [10,22,44–46], the reduction peak of the Ni@Al$_2$O$_3$-i catalyst above 659 °C is probably attributed to the NiAl$_2$O$_4$ species; the reduction peak at about 563–659 °C is mainly attributed to the nickel oxide which strongly interacts with the alumina shell, and the peak below 563 °C is attributed to the reduction of the inner core of the nanoparticle. Owing to the stronger interaction between the nickel particle and alumina shell in the Ni@Al$_2$O$_3$-i catalyst, the nickel particle was partially transformed into the NiAl$_2$O$_4$ spinel during the calcination process. However, the NiAl$_2$O$_4$ diffraction peaks are almost invisible on the XRD patterns of the calcined Ni@Al$_2$O$_3$-i catalyst. This is probably because that the diffraction peak intensity of the NiAl$_2$O$_4$ phase is much weaker than that of the NiO phase, and the XRD diffraction peaks corresponding to the NiAl$_2$O$_4$ phase are centered at $2\theta = 37.0°$, $45.0°$ and $65.5°$ (JCPDS: 10-0339), which are overlapped with the NiO diffraction peaks centered at $2\theta = 37.2°$, $43.3°$ and $62.8°$ (JCPDS: 73-1523). According to the H$_2$-TPR profile of the Ni@Al$_2$O$_3$-i catalyst, it is clear that the catalyst is not reduced sufficiently in the reduction process of the activity test, but during the reaction, the reducing environment may also contribute to the reduction of catalyst. In this study, all the reduction temperatures of the catalysts prior to the reaction are kept at 600 °C to compare the activity of different catalysts,
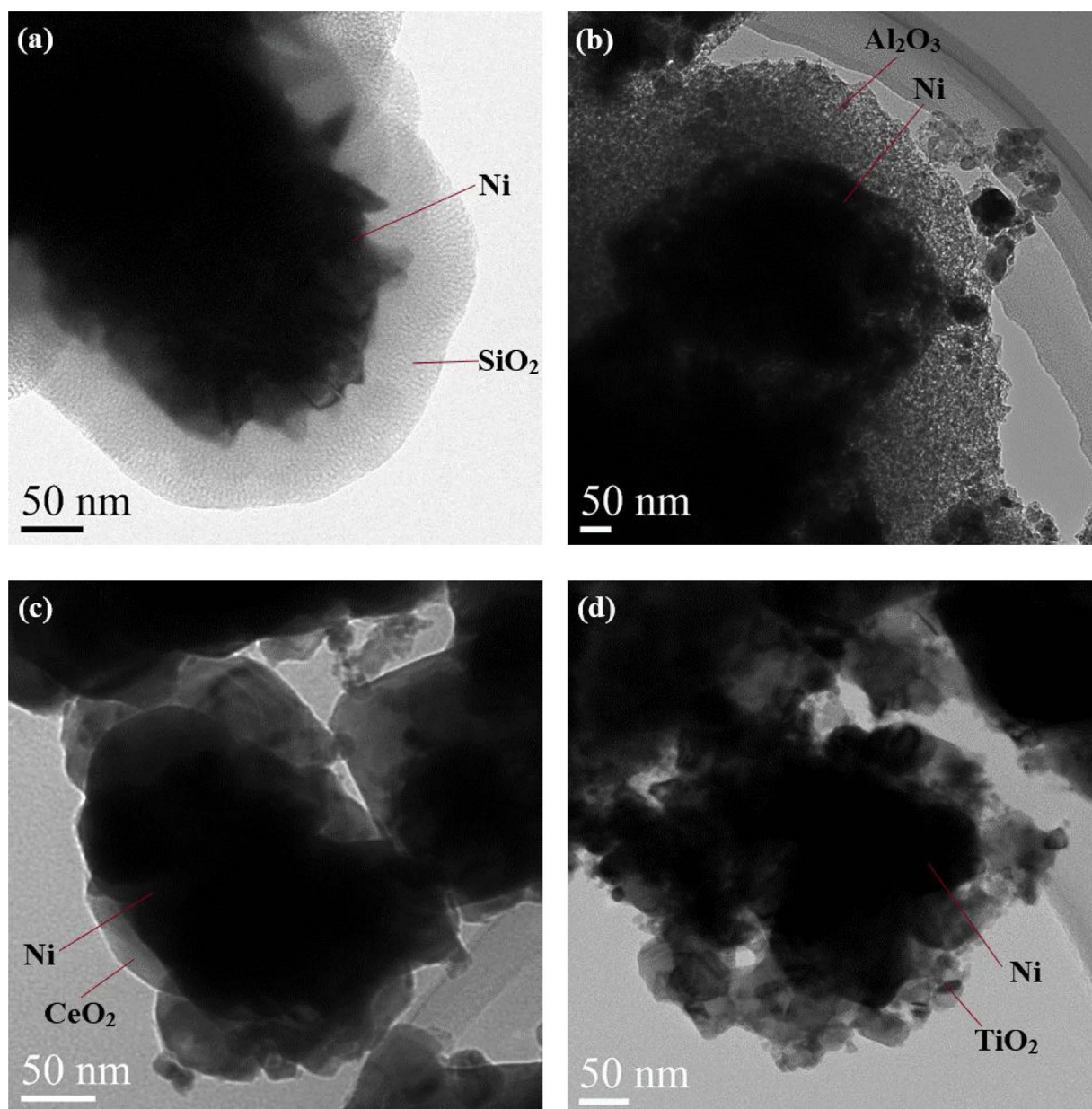
Fig. 3. TEM images of the core-shell catalysts reduced at 600 °C: (a) Ni@SiO$_2$, (b) Ni@Al$_2$O$_3$, (c) Ni@CeO$_2$, and (d) Ni@TiO$_2$.

and the effect of reduction temperature on the catalytic activity of Ni@Al$_2$O$_3$-*i* catalyst will be investigated in the future study.

3.2. Catalytic performance in the steam reforming of acetic acid

3.2.1. Effect of the shell thickness of the Ni@SiO$_2$ catalyst

The effect of shell thickness for the Ni@SiO$_2$ catalyst on the catalytic activity in the steam reforming of acetic acid was investigated. The hydrogen yields for the Ni@SiO$_2$ and Ni@SiO$_2$-T catalysts are presented in Fig. 7. There were no significant changes in the hydrogen yields for both the catalysts over the 10-h activity tests, suggesting the catalysts did not exhibit fouling. As expected, the Ni@SiO$_2$ catalyst showed a higher activity with a hydrogen yield of approximately 58% than Ni@SiO$_2$-T (53%) due to the effect of the silica shell thickness. This is because the thinner silica shell allows the reactants to more easily contact the nickel active sites in the steam reforming of acetic acid. The thicker shell makes the shell more robust and enhances the resistance to damage in the severe hydrothermal environment. On the other hand, the thicker shell increases the transfer resistance of reactants and products

through the shell.

3.2.2. Effect of the shell species

The conversions of acetic acid and the hydrogen yields in the steam reforming of acetic acid over the catalysts with different shell species are shown in Fig. 8. The reaction temperature is one of the most important factors that affects the conversion and hydrogen yield in the steam reforming of acetic acid. Relatively higher acetic acid conversions and hydrogen yields were obtained at a higher temperature due to the higher temperature favoring both the thermodynamics and kinetics of the steam reforming reaction. It is shown that the shell species greatly influence the catalytic activity in the steam reforming of acetic acid. As shown in Fig. 8a, the Ni@Al$_2$O$_3$ and Ni@CeO$_2$ catalysts show higher activities in the steam reforming of acetic acid with acetic acid conversions up to 98.8% and 97.3%, respectively. In contrast, the acetic acid conversions of Ni@SiO$_2$ and Ni@TiO$_2$ were much lower than those of Ni@Al$_2$O$_3$ and Ni@CeO$_2$, indicating the lower catalytic activities for the steam reforming of acetic acid. Meanwhile, these catalysts showed similar trends for their hydrogen yields (Fig. 8b). The activity in the
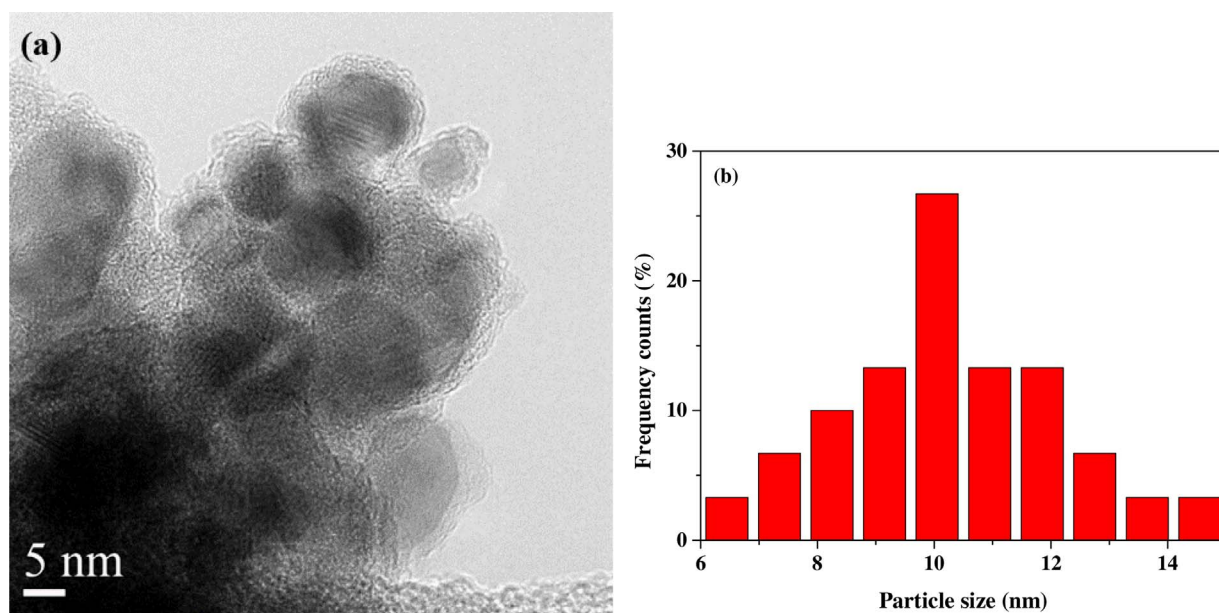
Fig. 4. (a) HRTEM image and (b) Ni particle size distribution of the Ni@Al$_2$O$_3$-*i* catalyst reduced at 600 °C.
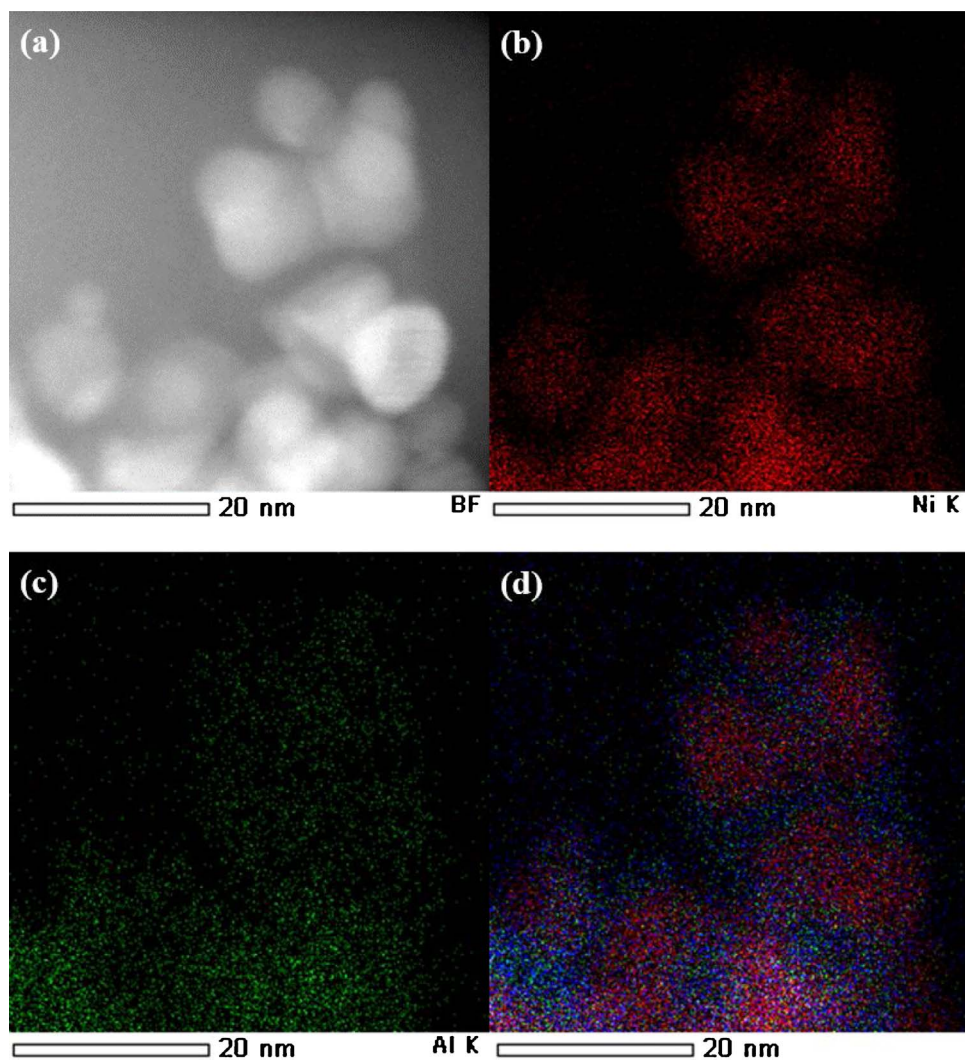

Fig. 5. STEM images and EDS mappings of the Ni@Al$_2$O$_3$-*i* catalyst reduced at 600 °C: (a) STEM images, (b) Ni mapping, (c) Al mapping, and (d) overlaid mapping. The blue section in (d) is O mapping. (For interpretation of the references to colour in this figure legend, the reader is referred to the web version of this article.)
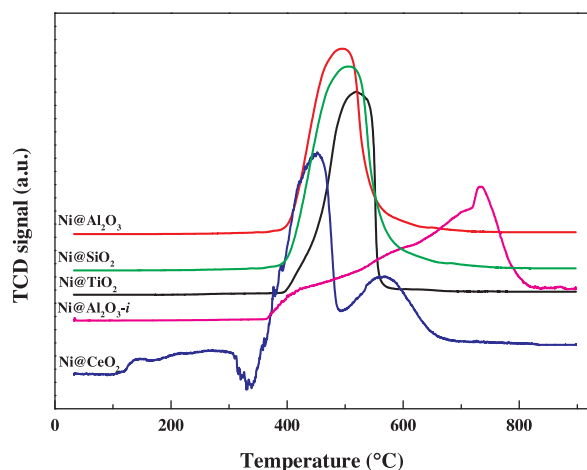
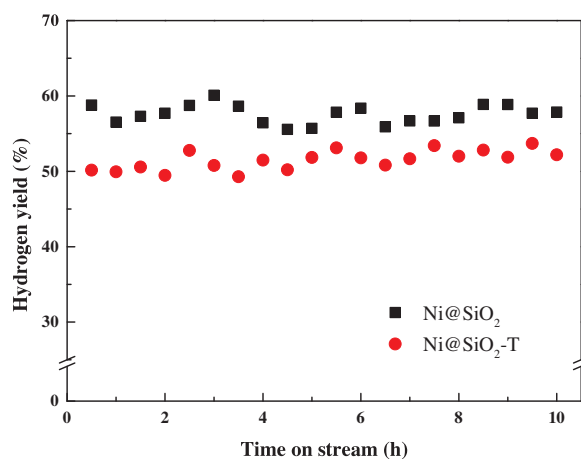**Fig. 6.** H₂-TPR profiles of the core-shell catalysts.

Fig. 7. Hydrogen yields of the Ni@SiO₂ and Ni@SiO₂-T catalysts for the steam reforming of acetic acid. Reaction conditions: 750 °C, atmospheric pressure, WHSV = 21 h^{-1}, and S/C = 3.18.

steam reforming of acetic acid decreased in the following trend: Ni@Al₂O₃ > Ni@CeO₂ > Ni@SiO₂ > Ni@TiO₂.

Ni@Al₂O₃ showed the highest activity for the steam reforming of acetic acid, which is explained by the properties of alumina. For the conventional supported catalyst, the activity of the steam reforming not only depends on the active sites but also depends on the type of support.

It was reported that the support also participates in the steam reforming reactions by dissociating water into ions [31,40,47]. Therefore, the type of support plays a key role in enhancing the activity of the steam reforming reactions [14,16,48,49]. According to previous studies [22,30,43,48], the Al₂O₃ support is the most widely used support for catalysts in the steam reforming reactions due to its ability to promote high activity and its high surface area. On the other hand, as discussed above, the prepared Ni@Al₂O₃ catalyst has a large surface area and highly porous structure according to the BET and TEM results, which is favorable for the adsorption and diffusion of reactants and products within the alumina shell. Although the Ni@CeO₂ catalyst had a low-porosity shell structure with a low surface area, it still showed a relatively high activity for the steam reforming of acetic acid, suggesting that CeO₂ has the potential to improve the catalytic activity of steam reforming. This is probably attributed to facile redox properties resulting from the oxygen vacancies in the CeO₂ lattice [43]. Although it has a highly porous silica shell structure, Ni@SiO₂ showed low activity for steam reforming. In previous research, Ni@SiO₂ showed good activity and stability in dry reforming and CO methanation reactions [35]. However, it is evidenced that Ni@SiO₂ is not suitable for the steam reforming reactions due to the great impact of the support on the catalytic activity. The Ni@TiO₂ catalyst showed the lowest activity for the steam reforming of acetic acid because of the poor enhancement of TiO₂ on the steam reforming reactions as well as the low-porosity shell structure.

It is concluded that Al₂O₃ is the most suitable shell for a catalyst in the steam reforming of acetic acid. However, the activity of Ni@Al₂O₃ is still much lower than the conventional NiRu/Al₂O₃ catalyst, which was prepared in our lab previously [43]. Therefore, it is necessary to further improve the catalytic activity of Ni@Al₂O₃.

3.2.3. Effect of the nickel particle size

The catalytic activity of Ni@Al₂O₃ was improved by decreasing the nickel particle size. As shown in Fig. 8a, the acetic acid conversion over Ni@Al₂O₃-i was higher than that over Ni@Al₂O₃, and the hydrogen yield over Ni@Al₂O₃-i was much larger than that over Ni@Al₂O₃ (Fig. 8b), indicating the catalytic activity of Ni@Al₂O₃ was greatly enhanced by decreasing the nickel particle size. The much larger increase of hydrogen yield than acetic acid conversion is mainly due to the different product distributions in the steam reforming of acetic acid over these two catalysts, as shown in Fig. 9. There was a larger ratio of CO₂ to CO and a smaller amount of CH₄ in the products over Ni@Al₂O₃-i, which are favorable for the formation of hydrogen. It is suggested that the smaller Ni particle not only provides more active sites for the steam reforming of acetic acid, but also promotes the WGS reaction (Eq. (2))
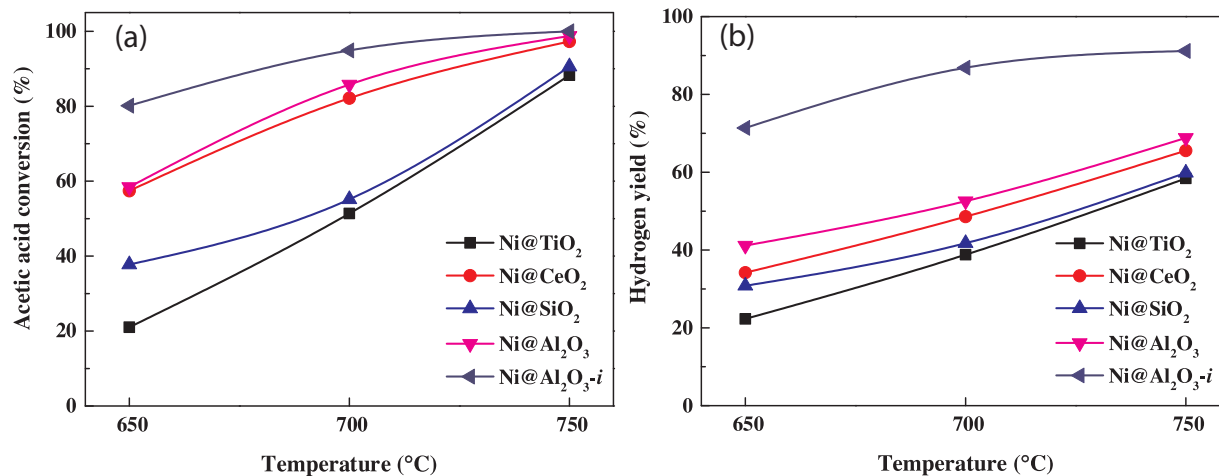

Fig. 8. (a) Conversions of acetic acid and (b) hydrogen yields in the steam reforming of acetic acid over different catalysts at various temperatures. Reaction conditions: atmospheric pressure, WHSV = 21 h^{-1}, and S/C = 3.18.
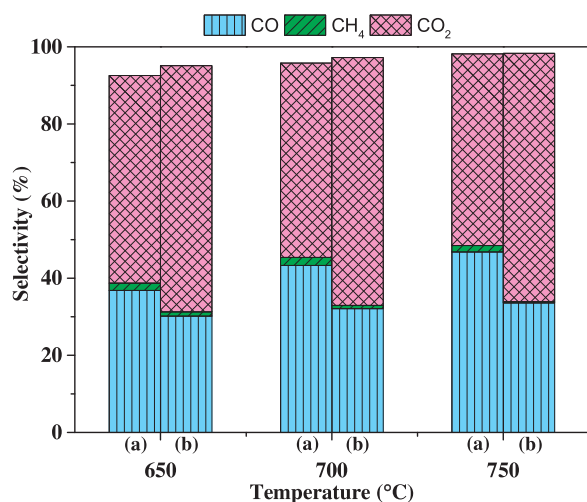
Fig. 9. Carbonaceous gas selectivity in the steam reforming of acetic acid over the (a) Ni@Al$_2$O$_3$ and (b) Ni@Al$_2$O$_3$-i catalysts at various temperatures. Reaction conditions: atmospheric pressure, WHSV = 21 h^{-1}, and S/C = 3.18.

and suppresses the formation of methane (Eq. (4)). It was reported that the transition metals such as Ni, Co also showed catalytic effect on the WGS reaction [14]. High temperature enhances the steam reforming of acetic acid, but impedes the exothermic decomposition reaction (Eq. (4)) and WGS reaction (Eq. (2)), showing a low selectivity of CH$_4$ and a small CO$_2$/CO ratio in the products. Moreover, the carbon formation over Ni@Al$_2$O$_3$-i was also much lower than that over Ni@Al$_2$O$_3$. Ni@Al$_2$O$_3$-i showed excellent catalytic activity in the steam reforming of acetic acid with a hydrogen yield up to 71.4% even at 650 °C. This is attributed to the much larger contact surface area of the smaller sized Ni particles, which provided more active sites for the steam reforming of acetic acid. On the other hand, the higher contact surface area also made the interaction between nickel and the alumina shell stronger.

HRTEM images of the spent Ni@Al$_2$O$_3$-i catalyst are presented in Fig. 10. The nickel particles are encapsulated by the amorphous alumina shell. It is obvious that the nickel particles of the spent Ni@Al$_2$O$_3$-i catalyst did not suffer from metal agglomeration in the severe hydrothermal environment, indicating the alumina shell can well protect nickel from sintering. Moreover, as shown in Fig. 10b, the alumina shell
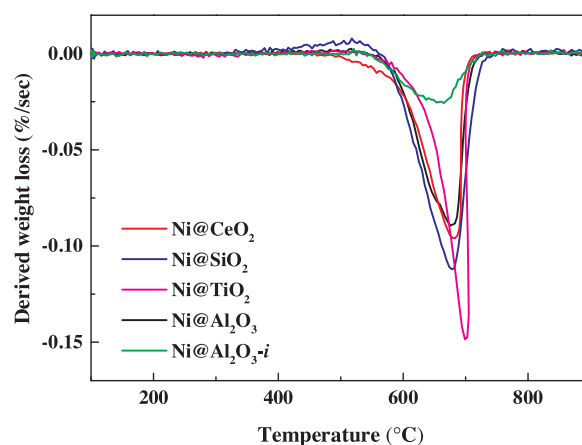

Fig. 11. DTG profiles of the spent catalysts. Air flow: 50 ml/min.

Table 3
Coke formation on the spent core-shell catalysts after the activity tests.

Catalyst	Ni@Al$_2$O$_3$-i	Ni@Al$_2$O$_3$	Ni@CeO$_2$	Ni@SiO$_2$	Ni@TiO$_2$
Weight loss (%)	15.2	42.0	44.1	45.1	46.3

of the spent Ni@Al$_2$O$_3$-i catalyst remained intact and did not undergo destruction or collapse after the catalytic activity test, suggesting the prepared alumina shell is rather robust and has excellent hydrothermal stability.

3.2.4. Coke formation

The coke formed on the catalyst after the activity test was analyzed by DTG (Fig. 11). According to the DTG profiles of the coked catalysts, all the coke combustion peaks were centered at approximately 700 °C, corresponding to graphitic carbon [50]. This indicates the coke formed on all the core-shell catalyst has the same properties, suggesting similar coke formation mechanisms for all the catalysts in the steam reforming of acetic acid. As shown in Table 3, the amount of coke formed on the core-shell catalysts synthesized using hydrazine only showed slight increases along with decreased activities as compared to the other samples, while the coke amount on Ni@Al$_2$O$_3$-i was rather small,
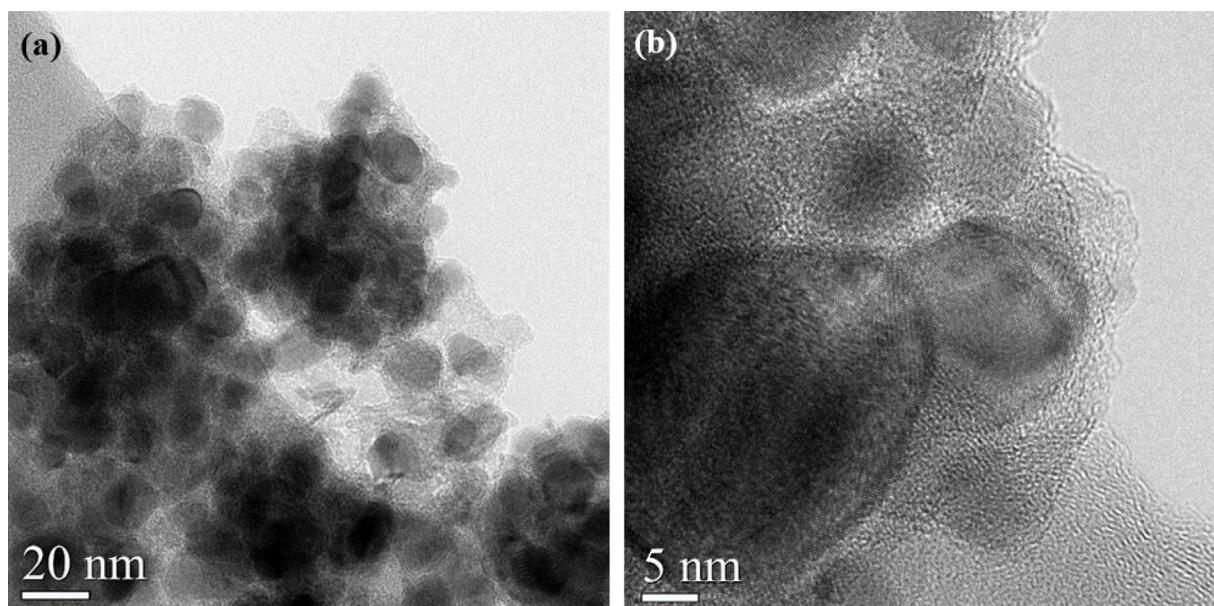

Fig. 10. HRTEM images of the spent Ni@Al$_2$O$_3$-i catalyst after the activity test: (a) low magnification and (b) high magnification.
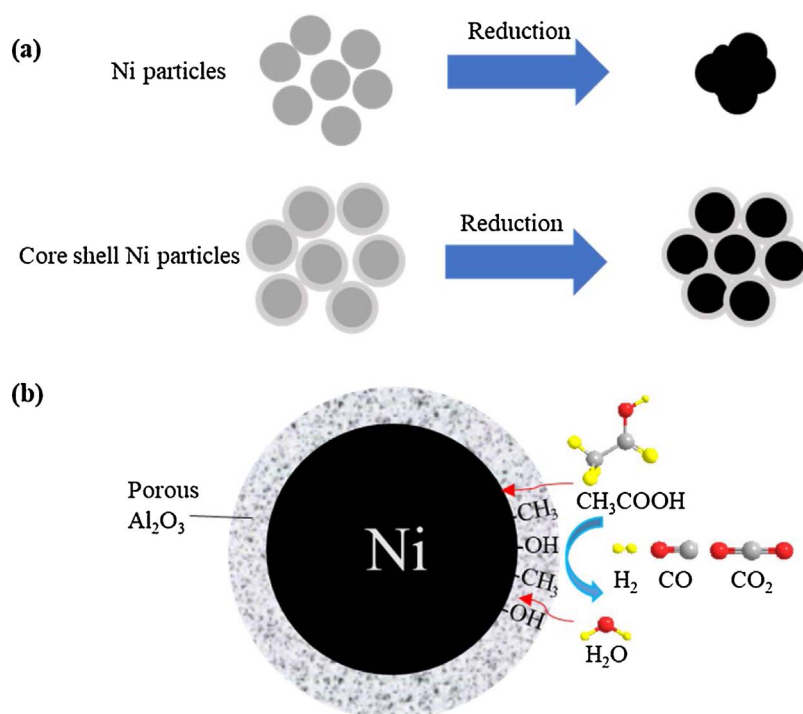
Fig. 12. Schematic illustrations of (a) the Ni sintering inhibition of the core-shell catalysts and (b) the acetic acid steam reforming mechanism over the Ni@Al$_2$O$_3$-*i* catalyst.

indicating the good resistance to coke formation in the steam reforming of acetic acid. The coke inhibition ability is attributed to the high catalytic activity of Ni@Al$_2$O$_3$-*i* for steam reforming, which greatly reduced the accumulation of coke precursors and unreacted acetic acid. Meanwhile, the side reactions, such as thermal decomposition of acetic acid, were also inhibited.

Fig. 12 shows schematic illustrations of the inhibition of nickel sintering for the core-shell catalysts and the mechanism of the steam reforming of acetic acid over the Ni@Al$_2$O$_3$-*i* catalyst. As shown in Fig. 12a, the bare nickel particles are agglomerated easily once reduced at a high temperature due to the large contact area. However, the contact surface between the nickel active sites and the reactants is greatly maintained for the core-shell catalysts due to the protection of the robust shell structure. Therefore, even under the severe reaction conditions during the steam reforming of acetic acid, the core-shell catalysts always show superior resistances to the Ni sintering. As shown in Fig. 12b, the main difference between the core-shell catalysts and the supported catalysts is that the reactants, i.e., acetic acid and water, must diffuse to the nickel surface through the shell. The porous alumina provides good permeability for the diffusion of the reactants. Due to the excellent water dissociation ability of alumina, much more dissociated water is concentrated on the nickel surface, which greatly improves catalytic activity in the steam reforming of acetic acid.

4. Conclusions

A series of nickel core-shell catalysts with various shell species, i.e., SiO$_2$, Al$_2$O$_3$, CeO$_2$ and TiO$_2$, were prepared. All these core-shell catalysts during reduction at 600 °C showed good resistance to nickel sintering. It was demonstrated that the core-shell catalysts could be used in the steam reforming of acetic acid. The Ni@SiO$_2$ catalyst with a thin silica shell showed better activity than its counterpart with a thick shell, suggesting the thin shell is favorable for the diffusion of reactants through the shell. By comparing the catalytic activities of the catalysts with various shell materials, it was concluded that the Ni@Al$_2$O$_3$ catalyst was the most suitable for the steam reforming of acetic acid, showing much higher catalytic activity than the other catalysts. This indicates that alumina has a better water dissociation ability than the other shell materials in the steam reforming reactions. Ni@Al$_2$O$_3$-*i*

showed excellent activity in the steam reforming of acetic acid with high hydrogen yield owing to its much smaller nickel particle size. At the same time, the coke amount formed on Ni@Al$_2$O$_3$-*i* was much smaller than that on the other catalysts. This was explained by the high catalytic activity of Ni@Al$_2$O$_3$-*i* in the steam reforming, which decreased the accumulation of the coke precursor. Based on the results observed by HRTEM, there were no significant changes of the core-shell structure of Ni@Al$_2$O$_3$-*i* before and after the reaction, implying that the prepared porous alumina shell had excellent hydrothermal stability.

References

[1] N. Chen, S. Gong, H. Shirai, T. Watanabe, E.W. Qian, Appl. Catal. A 466 (2013) 105–115.
[2] F. Lónyi, J. Valyon, E. Someus, J. Hancsók, Fuel 112 (2013) 23–30.
[3] S. Kelkar, C.M. Saffron, K. Andreassi, Z. Li, A. Murkute, D.J. Miller, T.J. Pinnavaia, R.M. Kriegel, Appl. Catal. B 174 (2015) 85–95.
[4] H.-W. Kim, K.-M. Kang, H.-Y. Kwak, J.H. Kim, Chem. Eng. J. 168 (2011) 775–783.
[5] E.C. Vagia, A.A. Lemonidou, J. Catal. 269 (2010) 388–396.
[6] M. Nurul Islam, R. Zailani, F. Nasir Ani, Renew. Energy 17 (1999) 73–84.
[7] T. Hoang, B. Geerdink, J. Sturm, L. Lefferts, K. Seshan, Appl. Catal B 163 (2015) 74–82.
[8] D. Wang, D. Montané, E. Chornet, Appl. Catal A 143 (1996) 245–270.
[9] L. An, C. Dong, Y. Yang, J. Zhang, L. He, Renew Energy 36 (2011) 930–935.
[10] F.G.E. Nogueira, P.G.M. Assaf, H.W.P. Carvalho, E.M. Assaf, Appl. Catal B 160–161 (2014) 188–199.
[11] Y.-X. Ran, Z.-Y. Du, Y.-P. Guo, J. Feng, W.-Y. Li, Appl. Surf. Sci. 400 (2017) 97–109.
[12] Z.-Y. Du, Y.-X. Ran, Y.-P. Guo, J. Feng, W.-Y. Li, Appl. Surf. Sci. 419 (2017) 114–125.
[13] B. Matas Güell, I. Babich, K.P. Nichols, J.G.E. Gardeniers, L. Lefferts, K. Seshan, Appl. Catal. B 90 (2009) 38–44.
[14] G. Chen, J. Tao, C. Liu, B. Yan, W. Li, X. Li, Renew. Sustainable Energy Rev. 79 (2017) 1091–1098.
[15] J. Sehested, J.A.P. Gelten, S. Helveg, Appl. Catal A 309 (2006) 237–246.
[16] A. Ochoa, I. Barbarias, M. Artetxe, A.G. Gayubo, M. Olazar, J. Bilbao, P. Castaño, Appl. Catal. B 209 (2017) 554–565.
[17] C. Rioche, S. Kulkarni, F.C. Meunier, J.P. Breen, R. Burch, Appl. Catal. B 61 (2005) 130–139.
[18] T. Hou, B. Yu, S. Zhang, J. Zhang, D. Wang, T. Xu, L. Cui, W. Cai, Appl. Catal. B 168–169 (2015) 524–530.
[19] F. Bossola, C. Evangelisti, M. Allieta, R. Psaro, S. Recchia, V. Dal Santo, Appl. Catal. B 181 (2016) 599–611.
[20] A.A. Lemonidou, E.C. Vagia, J.A. Lercher, ACS Catal. 3 (2013) 1919–1928.
[21] C.-j. Liu, J. Ye, J. Jiang, Y. Pan, ChemCatChem 3 (2011) 529–541.
[22] K. Kamonsuangkasem, S. Therdthianwong, A. Therdthianwong, N. Thammajak, Appl. Catal. B 218 (2017) 650–663.
[23] V. Shanmugam, R. Zapf, S. Neuberg, V. Hessel, G. Kolb, Appl. Catal. B 203 (2017)

859–869.

[24] L.F. Bobadilla, A. Álvarez, M.I. Domínguez, F. Romero-Sarria, M.A. Centeno, M. Montes, J.A. Odriozola, Appl. Catal. B 123 (2012) 379–390.
[25] A.H. Braga, E.R. Sodré, J.B.O. Santos, C.M. de Paula Marques, J.M.C. Bueno, Appl. Catal. B 195 (2016) 16–28.
[26] C. Montero, A. Ochoa, P. Castaño, J. Bilbao, A.G. Gayubo, J. Catal. 331 (2015) 181–192.
[27] W. Xu, Z. Liu, A.C. Johnston-Peck, S.D. Senanayake, G. Zhou, D. Stacchiola, E.A. Stach, J.A. Rodriguez, ACS Catal. 3 (2013) 975–984.
[28] Z. Gao, M. Dong, G. Wang, P. Sheng, Z. Wu, H. Yang, B. Zhang, G. Wang, J. Wang, Y. Qin, Angew. Chem. Int. Ed. 54 (2015) 9006–9010.
[29] G. Wu, S. Li, C. Zhang, T. Wang, J. Gong, Appl. Catal. B 144 (2014) 277–285.
[30] J. Remón, J.A. Medrano, F. Bimbela, L. García, J. Arauzo, Appl. Catal. B 132–133 (2013) 433–444.
[31] A. Ishihara, E.W. Qian, I.N. Finahari, I.P. Sutrisna, T. Kabe, Fuel 84 (2005) 1462–1468.
[32] E. Baktash, P. Littlewood, R. Schomäcker, A. Thomas, P.C. Stair, Appl. Catal. B 179 (2015) 122–127.
[33] Z. Li, M. Li, Z. Bian, Y. Kathiraser, S. Kawi, Appl. Catal. B 188 (2016) 324–341.
[34] J. Zhang, F. Li, Appl. Catal. B 176–177 (2015) 513–521.
[35] M.A. Lucchini, A. Testino, A. Kambolis, C. Proff, C. Ludwig, Appl. Catal. B 182 (2016) 94–101.
[36] S. Takenaka, H. Umebayashi, E. Tanabe, H. Matsune, M. Kishida, J. Catal. 245 (2007) 392–400.
[37] L. Li, S. He, Y. Song, J. Zhao, W. Ji, C.-T. Au, J. Catal. 288 (2012) 54–64.
[38] W. Li, D. Zhao, Adv. Mater. 25 (2013) 142–149.
[39] D.H. Kim, S.Y. Kim, S.W. Han, Y.K. Cho, M.-G. Jeong, E.J. Park, Y.D. Kim, Appl. Catal. A 495 (2015) 184–191.
[40] S. Thaicharoensutcharittham, V. Meeyoo, B. Kitiyanan, P. Rangsunvigit, T. Rirksomboon, Catal. Today 164 (2011) 257–261.
[41] M.A. Lucchini, A. Testino, C. Ludwig, A. Kambolis, M. El-Kazzi, A. Cervellino, P. Riani, F. Canepa, Appl. Catal. B 156 (2014) 404–415.
[42] H. Li, H. Lin, Y. Hu, H. Li, P. Li, X. Zhou, J. Mater. Chem. 21 (2011) 18447–18453.
[43] J. Pu, F. Ikegami, K. Nishikado, E.W. Qian, Int. J. Hydrogen Energy 42 (2017) 19733–19743.
[44] G. Wu, C. Zhang, S. Li, Z. Huang, S. Yan, S. Wang, X. Ma, J. Gong, Energy Environ. Sci. 5 (2012) 8942–8949.
[45] A. Iriondo, V.L. Barrio, J.F. Cambra, P.L. Arias, M.B. Guemez, M.C. Sanchez-Sanchez, R.M. Navarro, J.L.G. Fierro, Int. J. Hydrogen Energy 35 (2010) 11622–11633.
[46] F. Bimbela, J. Ábrego, R. Puerta, L. García, J. Arauzo, Appl. Catal. B 209 (2017) 346–357.
[47] K. Takanabe, K.i. Aika, K. Inazu, T. Baba, K. Seshan, L. Lefferts, J. Catal. 243 (2006) 263–269.
[48] S. Goicoechea, E. Kraleva, S. Sokolov, M. Schneider, M.-M. Pohl, N. Kockmann, H. Ehrich, Appl. Catal. A 514 (2016) 182–191.
[49] N. Iwasa, T. Yamane, M. Takei, J.-i. Ozaki, M. Arai, Int. J. Hydrogen Energy 35 (2010) 110–117.
[50] R. Bajpai, L. Rapoport, K. Amsalem, H.D. Wagner, CrystEngComm 18 (2016) 230–239.